


Nonreciprocal Epsilon-Near-Zero-Dielectric Bilayers: Enhancement of Nonreciprocity from a Nonlinear Transparent Conducting Oxide Thin Film at Epsilon-Near-Zero Frequency

Diego M. Solís¹ and Nader Engheta^{1*}

Department of Electrical and Systems Engineering, University of Pennsylvania, Philadelphia, Pennsylvania, USA

 (Received 25 August 2021; revised 31 January 2022; accepted 17 February 2022; published 22 March 2022)

We envision the use of an indium tin oxide (ITO) thin film as part of a bilayered silicon-photonics subwavelength device to boost nonlinearity-assisted all-passive and ultrafast nonreciprocal behavior. Asymmetric p -polarized oblique excitation of a mode near the epsilon-near-zero frequency, with a highly confined and enhanced normal electric field component and large absorption, allows one to harness the strong subpicosecond nonlinear response of ITO for the generation of notable nonreciprocal performance in an ultracompact two-port element. Although the results are limited by loss, we find the optimal operational point and the maximum attainable nonreciprocal transmittance ratio of the metasurface versus light intensity—including an apparent upper bound slightly over 2—and we perform exhaustive numerical simulations considering nonlinear processes of both anharmonic and thermal nature that validate our predictions, including steady-state and pulsed-laser excitation.

DOI: [10.1103/PhysRevApplied.17.034053](https://doi.org/10.1103/PhysRevApplied.17.034053)

I. INTRODUCTION

The nonreciprocal propagation of light (implying, e.g., that in a two-port system the transmission is different when the system is excited from opposite sides) is a key ingredient in the pursuit of all-optical nanocircuits. Lorentz reciprocity can be broken with (i) some form of time-reversal-antisymmetric biasing [1] (which may be magneto-optical [2–4] or, in the subterahertz regime, a transistor biasing network [5,6]), (ii) spatially inhomogeneous temporal modulation [7–14], or (iii) nonlinear optical transitions [15–24], the latter being the only option that allows an all-passive approach [although it can also be leveraged to pursue nonreciprocal transmission contrast with, e.g., \mathcal{PT} -symmetric (active) systems [25–27]]. Its operation principle consists of bringing together geometrical asymmetry and some sort of nonlinearity (typically Kerr-like): given that the field distribution inside such an asymmetric structure varies with the excitation port, so does the nonlinear response and thus the transmission. In this paper, we propose to boost this nonlinear mechanism through the use of an indium tin oxide (ITO) thin layer at its epsilon-near-zero (ENZ) frequency as part of a silicon-ITO two-port device. We show that, when such a structure is quasisonantly excited under oblique p -polarized light, the strong (nonresonant) ENZ nonlinear response dramatically increases the nonreciprocal transmission.

Now, although it is known from the findings in Ref. [28] that a (passive) nonlinear diode shows “dynamic reciprocity”—i.e., it behaves as reciprocal when it is perturbed by a forward-propagating (pump) pulse—and hence cannot be used as an isolator [29] (although some alternative routes have recently been proposed to alleviate this limitation, based on chiral cross-Kerr nonlinearities [30,31] or photorefractive-induced quadrature-phase-shifted gratings [32]), nonlinearity-induced platforms are still distinctly appealing for the nonreciprocal transmission of pulsed signals, besides the fact that the simplicity of their architecture results in photonic integration and scaling, particularly as compared with the complex (and, at least, wavelength-scale) circuitry needed for (active) spatiotemporal modulation [8,13]. On the subject of pulsed routing, high-speed operation is challenging [20,22] and is hindered by the dynamics of the nonlinear response, and this is where ENZ transparent conducting oxides (TCOs) excel: the unparalleled interest they are attracting as nonlinear materials does not hinge on the strength of their $\chi^{(3)}$ in itself, which is certainly not larger than what can be found for resonant interband nonlinearities of bound electrons (such as, e.g., saturable absorption) in more conventional (and with possibly less linear absorption) dielectric and semiconductor materials [33]. What makes TCOs exceptional is the conjunction of large nonlinearity, speed (certainly faster than, e.g., free-carrier dispersion and absorption generated via two-photon absorption in silicon [20], and even more so with respect to the thermo-optic effect [16]) due to the nonresonant intraband

*engheta@ee.upenn.edu

nonlinearity of the free electrons [34,35], and wide optical bandwidth.

With respect to the last point, and beyond the intrinsic bandwidth-related nature of the nonlinear transitions (Kerr in some cases), nonreciprocal passive platforms typically rely on one or more high- Q cavities to extrinsically strengthen the nonlinear response [16,19–22], in combination with some form of Fano resonance. These structures can provide a large nonreciprocal intensity range—and, as the number of nonlinear resonators increases, they can do so for larger levels of forward transmission [36,37]—and, relevantly, bistability, but their highly resonant character entails a very narrowband range of operation (approximately 1 nm in the near infrared): the ubiquitous gain-bandwidth compromise. Our proposed bias-free quasiresonant metasurface, on the other hand, is fairly broadband, and thus the broadband character is at the expense of weaker nonreciprocal responses. In addition, it shows further advantages, namely the above-mentioned salient features of ultracompactness, ultrashort response delay, and extreme simplicity of fabrication.

II. PROOF OF CONCEPT

Our proposed idea is shown schematically in simplified form in Fig. 1(a) for a silicon-ENZ bilayer infinitely extended in the transverse y and z directions at normal incidence: the structural asymmetry brought about by the two stacks gives rise to different electric field strengths inside the ENZ nonlinear layer (more details of the physics of the nonlinearities under consideration can be found in the following) when port 1 or 2 is excited, and thus gives rise to different strengths of the nonlinear response that, in turn, alter the transmission coefficients differently. Now, it turns out that time-reversal symmetry and thermodynamics dictate that, for any linear structure, the field-distribution asymmetry for excitation from opposite ports is inversely proportional to the transmission [17,36]; as pointed out in Refs. [38–40], the ratio of field distributions $|\mathbf{E}_{12}|^2/|\mathbf{E}_{21}|^2$ for an arbitrary two-port lossless linear network is bounded by $(1-R)/(1+R) \leq |\mathbf{E}_{12}|^2/|\mathbf{E}_{21}|^2 \leq (1+R)/(1-R)$, where $R = |s_{11}| = |s_{22}|$, and where \mathbf{E}_{ij} is the electric field inside the structure when it is excited from port j (i being the output port). As a proof of concept, this behavior, showing a trade-off between the nonreciprocal transmission ratio (NTR) and insertion loss, is illustrated in Fig. 1, where we first assume a nonlinear nondispersive (lossless) ENZ material, with a dielectric permittivity set in our toy model to $\epsilon_{\text{ENZ}} = 0.1$: this arbitrary value is justified by the fact that, for a given nonlinear susceptibility $\chi^{(3)}$ (we consider Kerr-like instantaneous third-order processes only here), the material has an effective nonlinear response that increases with decreasing ϵ [41].

The origin of the above-mentioned trade-off is clearly seen in Figs. 1(b1) and 1(b2) as a function of the

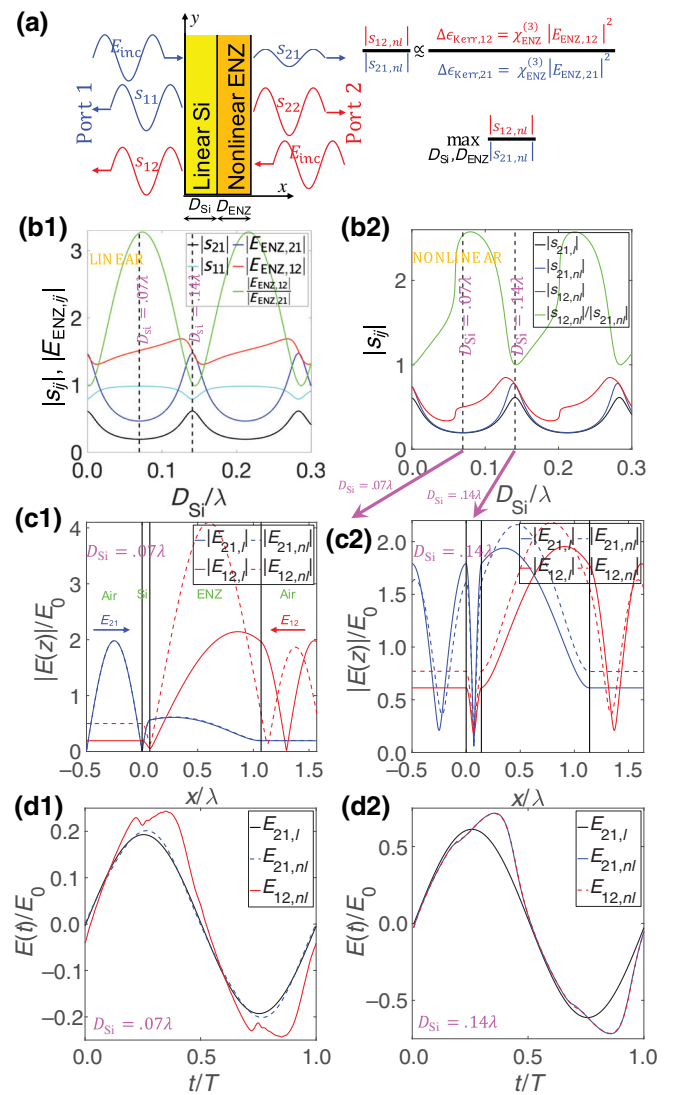


FIG. 1. Toy model of nondispersive nonreciprocal bilayer device. (a) Schematic plot of the asymmetric nonlinear bilayer two-port device. (b1) s -parameters and x -averaged electric field magnitude inside the ENZ slab as a function of the thickness D_{Si} of the silicon layer in the linear problem. (b2) Transmission coefficients versus D_{Si} in the nonlinear nonreciprocal problem [$\chi^{(3)} = 3.33 \times 10^{-21}$ (V/m) $^{-2}$, $E_0 = 10^9$ V/m]. (c1), (c2) Magnitude of electric field phasor versus x in the monochromatic nonlinear problem when D_{Si} minimizes (c1) and maximizes (c2) $|s_{21}|$. (d1), (d2) Electric field at the output plane versus time in the harmonic generation nonlinear problem.

thickness D_{Si} of the Si layer (D_{ENZ} is arbitrarily fixed at one free-space wavelength λ for this proof of principle): in Fig. 1(b1), the solution to the linear problem under normally incident plane-wave excitation is analytically derived by the usual transfer-matrix method (TMM) [42,43] of electromagnetic transmission-line theory and shows how the ratio of x -averaged electric field magnitudes inside the ENZ layer $|E_{\text{ENZ},12}|/|E_{\text{ENZ},21}|$ (green line)

has its first maximum very close to the first minimum of the transmission (black line, $|s_{21}| = |s_{12}|$) at $D_{\text{Si}} = 0.0695\lambda$, whereas this ratio is first equal to 1 at (in addition to $D_{\text{Si}} = 0$) $D_{\text{Si}} = \lambda/2\sqrt{\epsilon_{\text{Si}}}$ ($\epsilon_{\text{Si}} = 12.36$), also very close to the first maximum of the transmission at $D_{\text{Si}} = 0.1477\lambda$. In Fig. 1(b2), we consider the (monochromatic) nonlinear problem parameterized by $\chi^{(3)}(\omega; \omega, -\omega, \omega) = 3.33 \times 10^{-21} \text{ (V/m)}^{-2}$ [i.e., only the self-phase-modulation (SPM) process is taken into account [44]; in this regard, we would like to emphasize that the magnitude of our $\chi^{(3)}$ in this first proof-of-concept dispersionless scenario is arbitrarily small; the next sections do include dispersion, and tackle $\chi^{(3)}$ in detail]. We find s_{21} and s_{12} by a nonlinear finite-difference frequency-domain (FDFD) method [45] for an electric-field-phasor strength of $E_0 = 10^9 \text{ V/m}$, which show a NTR of $|s_{12,nl}|/|s_{21,nl}|$ (green line) that is precisely maximized (minimized) around $D_{\text{Si}} = 0.0695\lambda$ ($D_{\text{Si}} = 0.1477\lambda$), in agreement with $|E_{\text{ENZ},12}|/|E_{\text{ENZ},21}|$ in Fig. 1(b1). Figures 1(c1) and 1(c2) show, for these two thicknesses of interest, the electric field profiles versus x in the linear and nonlinear scenarios under forward and backward transmission. Whereas in Fig. 1(c1) $|E_{21,l}(x)| \ll |E_{12,l}(x)|$, and thereby the nonlinear response, is perturbative in the forward direction, in Fig. 1(c2) $|E_{21,l}(x)|$ and $|E_{12,l}(x)|$ inside the ENZ slab are essentially mirror images of each other, and, consequently, so are $|E_{21,nl}(x)|$ and $|E_{12,nl}(x)|$, which leads to a NTR of approximately 1 (the subscripts l and nl stand for “linear” and “nonlinear,” respectively). Figures 1(d1) and 1(d2) further exemplify this nonreciprocal transmission when we consider an instantaneous—it cannot be otherwise in a lossless material [44]—nonlinear polarization of the form $P_{nl}(z, t) = \epsilon_0 \chi^{(3)} E^3(z, t)$, which also accounts for, e.g., harmonic generation processes such as $(3\omega; \omega, \omega, \omega)$. We address this nonlinear polarization by a nonlinear finite-difference time-domain method [46] and plot the temporal profile of the resulting transmitted electric field for excitation from opposite ports for the two thicknesses of interest: whereas in Fig. 1(d1) $E_{12,nl}$ shows a much larger high-harmonic content than the perturbatively nonlinear output $E_{21,nl}$, in Fig. 1(d2) we have that $E_{12,nl} \approx E_{21,nl}$, and harmonic distortion is notable for both forward and backward incidence. Interestingly, if we were to increase D_{ENZ} much further, we would see modulation instability and even chaotic behavior, given that our toy model is nondispersive and therefore phase-matched [41]; this phenomenon is already starting to emerge in $E_{12,nl}$ in Fig. 1(d1). (We note that we choose to neglect two-photon absorption and self-phase modulation in the silicon layer; this is justified because, as seen in the next section, the field enhancement takes place inside the ITO film. Additionally, the linear absorption of silicon can be made close to negligible if we redshift the wavelength of operation: the ITO deposition process can be used quite precisely to control the ENZ wavelength, up to approximately 1550 nm [47]. In

any case, other high-index dielectrics could be used instead of silicon.)

III. REALISTIC DESIGN WITH ITO

When we consider realistic materials and bring dispersion into the picture, the efficiency of the overall nonlinear response is damped by losses and, in the case of harmonic generation, by phase mismatch as well. Regardless, thin films of TCOs such as Al-doped ZnO [48] and ITO [49] have shown, in the frequency range of vanishing real part of their dielectric function, an unprecedentedly large effective nonlinear refractive index [48,49] and enhanced harmonic generation [47,50–52], especially for TM-polarized light under oblique incidence that maximizes the component of the electric field normal to the boundary, E_x [53]. This has been achieved by coupling the incident transverse wave either to the bound plasmon-polariton ENZ mode—in, e.g., the Kretschmann configuration as in Ref. [50]—or to the leaky Ferrell-Berreman mode derived from the longitudinal bulk plasmon resonance [47,51,54]. Following this reasoning, we adopt the latter approach and design a Si-ITO thin bilayer structure that simultaneously maximizes both the absorption and $|E_x|$ —the latter is approximately constant across the thickness of a (deeply) subwavelength film—in the linear problem at the ENZ frequency when the ITO port is fed (the permittivity of ITO is parameterized with a Drude model; see Appendix A for more details). For a moderate nonlinear responses, this operational point will thus be in the vicinity of a peak in the NTR. A maximum absorptance of 0.83 is found around $D_{\text{Si}} = 80 \text{ nm}$ and $D_{\text{ITO}} = 100 \text{ nm}$ in the usual 40° – 55° range.

With these two thicknesses, we move on to our nonlinear problem, but let us first compare, in Fig. 2, the absorptance [Figs. 2(a1) and 2(a2)] and the normal component of the electric field [Figs. 2(c1) and 2(c2)] when the optimized linear structure is excited from either side: when port 2 is excited, i.e., when the incident plane wave propagates from the right [shown in red in Fig. 1(a)] towards the ITO-air boundary [Figs. 2(a2) and 2(c2)], an absorption peak of 0.86 is achieved at $(\lambda, \theta) \approx (1214 \text{ nm}, 38.5^\circ)$, whereas the maximum enhancement of $|E_x|^2$ at the Si-ITO interface, equal to 3.39, is located at $(\lambda, \theta) \approx (1216 \text{ nm}, 47.5^\circ)$; we use this asymmetry in the field distribution with respect to excitation from port 1 in order to maximize the sought nonreciprocal response. Incidentally, note the slight shift in angle between the peaks of the absorption and $|E_x|$: these two peaks would tend to converge in a situation of perfect absorption, but such a circumstance would in this case be found only in connection with a virtual mode, i.e., an eigenmode that emerges when the modal dispersion diagram of the layered structure is analyzed in the complex frequency (or complex transverse-wave-vector) plane [55–57], that is, with an exponential profile either

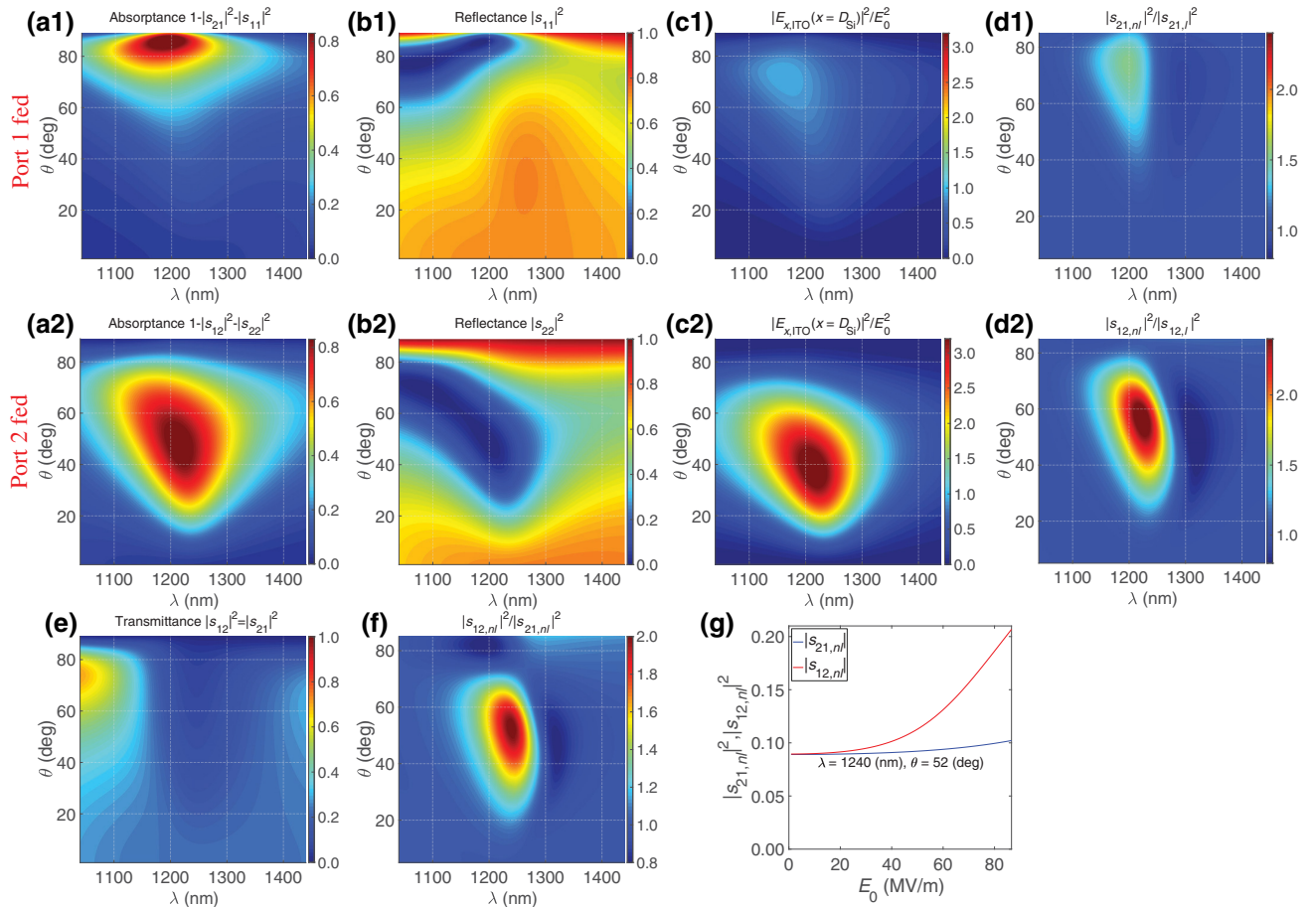


FIG. 2. Nonlinearity-induced nonreciprocal response versus (λ, θ) . (a1)–(d1) Linear absorbance, reflectance, normalized $|E_x(x = D_{Si})|$, and nonlinear-to-linear transmittance ratio, respectively, for excitation from port 1. (a2)–(d2) Similarly for port 2. (e), (f) Linear (reciprocal) transmittance and squared NTR, respectively. (g) Dependence of the nonlinear nonreciprocal response versus incident electric field for the optimal (λ, θ) point taken from (f), the optimal λ being precisely the ENZ wavelength.

in time or in the transverse direction. Additionally, the reflectance maps in Figs. 2(b1) and 2(b2) illustrate how the absorption peak more or less overlaps with a zero in the reflectivity and can thus be linked to the pseudo-Brewster angle. Restricting our nonlinear problem to SPM at the ENZ frequency for now and assuming a third-order nonlinear susceptibility $\chi^{(3)} = 6.67 \times 10^{-18} \text{ (V/m)}^{-2}$ (Appendix C explains in detail why we use such a value) and $E_0 = 8.66 \times 10^7 \text{ V/m}$, the nonlinear transmittance enhancements for both ports are mapped in Figs. 2(d1) and 2(d2), while the squared NTR is shown in Fig. 2(f), showing a maximum $|s_{12,nl}|^2/|s_{21,nl}|^2$ ratio of 2.04 at the point $(\lambda, \theta) \approx (1240 \text{ nm}, 52^\circ)$, i.e., exactly at the ENZ wavelength [note also that, for excitation from port 1, there is an absorbance peak of 0.93 close to grazing incidence at $(\lambda, \theta) \approx (1193 \text{ nm}, 86^\circ)$ that nonetheless, due to the low $|E_x|$ enhancement, leads to a maximum $|s_{12,nl}|^2/|s_{21,nl}|^2$ ratio of only 1.27]. Finally, we choose this point to measure the strength of the nonlinear nonreciprocal response versus the intensity of the incident light in

Fig. 2(g), where the nonlinearity in $|s_{12}|^2$ (red) is much stronger than that in $|s_{21}|^2$ (blue).

These nonlinear simulations are performed with the same one-dimensional (1D) FDFD solver as used for Fig. 1: for plane-wave oblique incidence, we can simplify the periodic boundary conditions across y and shrink the nonlinear monochromatic two-dimensional problem down to a 1D grid by simply enforcing $\partial/\partial y = ik_{y,\text{inc}}$ (with the $e^{-i\omega t}$ convention). Furthermore, above the intensity level given by the chosen E_0 , the Newton predictor-corrector iterative scheme of our nonlinear solver does not converge when $|E_x|$ is maximum at the pseudo-Brewster angle, which is perfectly consistent with an extremely large nonlinear polarization. [In time-domain solvers, at each time step and for each vector-field component and point in space, E is updated from D through, in the simplest case, $E = D/\epsilon_0(\epsilon_r + \chi^{(3)}E^2)$, by iterating with the value of E obtained from the previous iteration in the denominator, until a prescribed error tolerance is achieved (more details can be found in Ref. [46,58]). In the frequency domain,

an analogous approach can be adopted by extending this rationale to a matrix system.] In this regard, Appendix B shows how one could in principle achieve similar NTR values with dramatically less intensity by reducing the linear absorption coefficient of the ITO.

IV. NONRECIPROCAL RESPONSE TO A PULSED LASER BEAM

In the above section, we consider a realistic Drude-like dispersion for $\chi^{(1)}$ but narrow the nonlinear problem down to SPM at a single frequency in a steady state. A more realistic approach needs to consider (i) a richer ensemble of nonlinear processes—although quantifiably less significant than SPM in the case of TCOs [33,41,49]—and (ii) the dispersive nature of the relevant nonlinear susceptibilities. In Appendix C, we briefly go over how the origin of nonlinear processes in TCOs (including ITO) lies in the nonparabolicity of their conduction band, and make a distinction between fast (anharmonic) and slow (thermal) nonlinearities [33,59]: for our purposes, it suffices to neglect the dispersion of the former type of nonlinearity and consider the same instantaneous Kerr-like polarization response as in Sec. II, viz., $P_{\text{Kerr},j}(\mathbf{r}, t) = \epsilon_0 \chi^{(3)} E_j^3(\mathbf{r}, t)$, $j = x, y$ being the Cartesian component; in the latter type of nonlinearity, the “hot” plasma frequency $\omega_{p,h}$ is reduced through laser-induced heating [34,35], yielding an effective nonlinear susceptibility $\chi_{\text{eff}}^{(3)}$ 2 orders of magnitude larger. In this respect, an adequate comparison of these two effects is best done in the time domain, where all frequency-mixing processes are more easily simulated in the former case, and the delay effect in the latter case emerges. Moreover, high-power lasers hardly operate in a continuous-wave mode. Besides, the nonlinearity enhancement due to the low group velocity at the ENZ frequency [60] is now taken into account. We thus perform numerical experiments by exciting our proposed nonreciprocal structure with a high-intensity ultrafast pulse (see Appendix D for details). The setup of the numerical experiment is shown in Fig. 3(a), where we compare the normalized nonlinear transmission for both nonlinearities as a function of the laser intensity. For the sake of discussion, we again consider, for the Kerr interactions, $\chi^{(3)} = \text{Re}[\chi_{\text{eff}}^{(3)}]/3$, i.e., the fast and slow nonlinearities are (approximately) equally strong (see Appendix C). In Fig. 3(b), we show how the $|s_{12,nl}|^2/|s_{21,nl}|^2$ ratio reaches a maximum of around 2—commensurate with the results in the frequency domain in Fig. 2—at approximately $E_0 = 200$ MV/m (black and green solid lines). Interestingly, although beyond this field intensity the nonlinear response keeps increasing (blue and red plots), this tends to saturate, and the NTR decays. Importantly, we should mention that, as opposed to the characterization of the slow nonlinearity in Appendix C, saturation effects are in no way parameterized by a single instantaneous third-order susceptibility, and so one can at

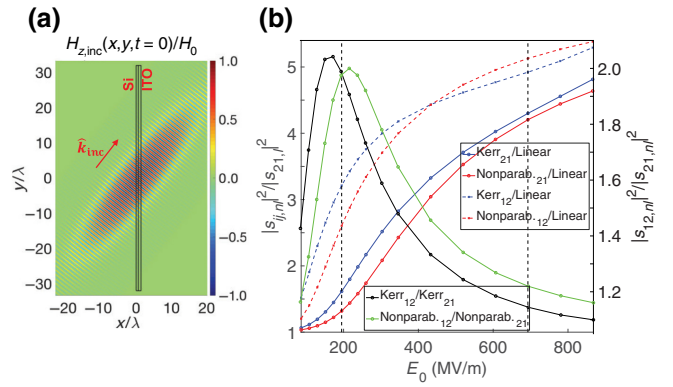


FIG. 3. Nonreciprocal response for excitation with an ultrafast pulse. (a) Schematic drawing of the setup of the numerical experiment for excitation from port 1, and superimposed incident magnetic field H_z when the maximum of the intensity crosses the middle point of the bilayer ($t = 0$). (b) Nonlinearity-induced nonreciprocal response versus incident electric field intensity [in fact, its phasor value halved, for comparison with Fig. 2(d)], assuming both Kerr-like (fast) and thermal (slow) nonlinearities: the blue and red (black and green) curves represent nonlinear-to-linear [nonlinear backward (12)-to-forward (21)] transmittance ratios, respectively.

most state that the Kerr nonlinear transmission (solid and dashed blue lines)—and not the Kerr nonlinear response *per se*—saturates in the range of intensities considered.

In Fig. 4, we look in detail into the case for which $E_0 = 195$ MV/m (first vertical dashed line in Fig. 3). Figure 4(a) shows, for the fast nonlinearity, the near-field maps of E_x and E_y when the incident Gaussian pulse is at its maximum ($t = 0$); strikingly, the enhancement of E_x when excitation happens from the ITO side is somewhat quenched in the harmonic generation process. This can be seen more clearly in Fig. 4(a2) when $E_x(y, t = 0)$ at the x -center of the ITO slab (dashed blue) is juxtaposed with the linear and nonparabolic-nonlinear cases (solid black and dashed red lines, respectively). The results included in Appendix E for a higher light intensity [see Fig. 9(a2)] replicate this behavior also for the thermal nonlinear process, confirming the intuition behind what is perhaps the key takeaway message: as seen in Fig. 3(b), there is a fundamental upper bound on the nonreciprocal response achievable with this structure, imposed by the simple fact that, as the nonlinear response increases or saturates, the mode confinement in the direction that excites the mode—and thus the asymmetry between opposite directions—tends to vanish (the permittivity of the ITO layer is dominated by self- and cross-phase modulation at large intensities [61], thus detuning the bilayer from optimal coupling conditions); in other words, the response tends to become reciprocal for very large optical intensities. The only open route to increasing the NTR further would be by reducing the loss and hence the baseline linear (reciprocal) transmission: in

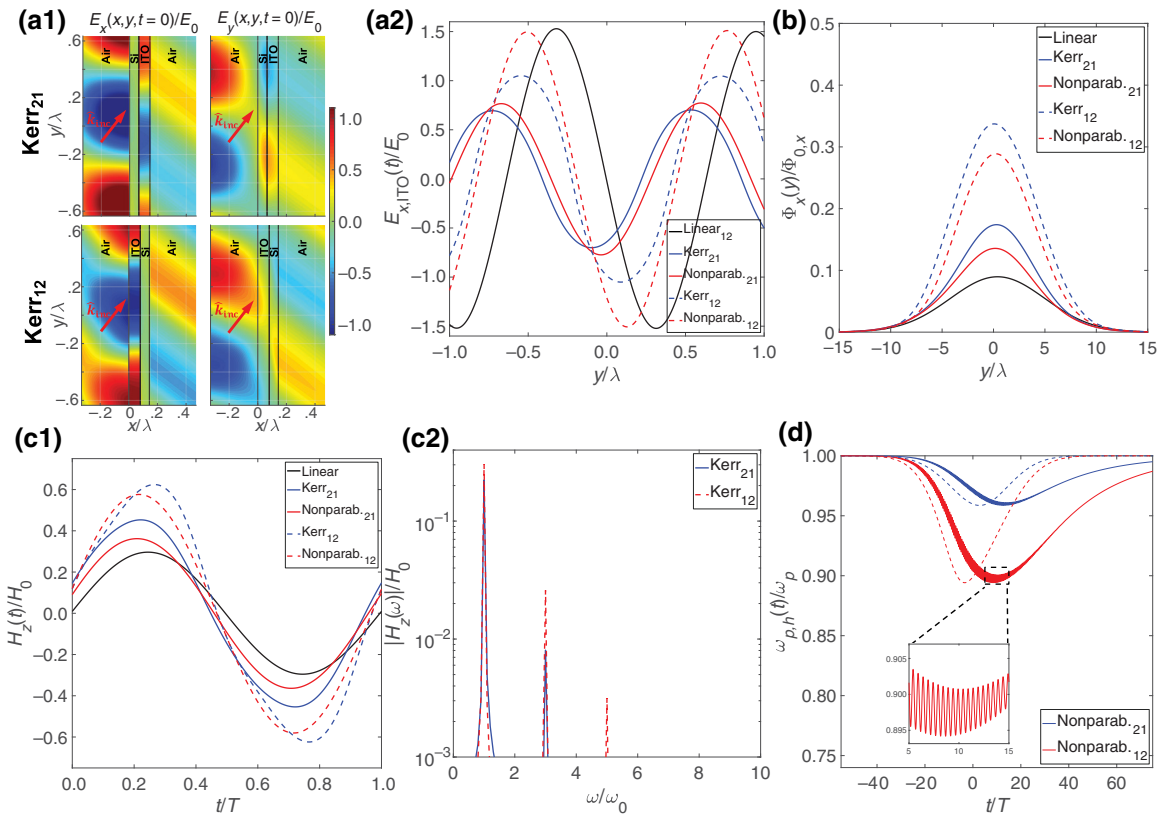


FIG. 4. Nonlinear response of the nonreciprocal device for maximum NTR: $E_0 = 195$ MV/m. (a1) x - y maps of (normalized) E_x and E_y at $t = 0$ for excitation from both ports, with Kerr nonlinearity only. (a2) 1D sections of E_x in the middle of the ITO film (at fixed x) and $t = 0$ vs y , but considering all linear, Kerr, and thermal scenarios. (b) Normalized flux of energy density across the output plane of the bilayer (Φ_x vs y) corresponding to the scenarios in (a2). (c1) Time profile of (normalized) transmitted H_z at $y = 0$ (i.e., very close to the beam axis). (c2) Spectral content of the Kerr signals in (c1), with third and fifth harmonics showing up. (d) Time-varying nonlinear (thermal) plasma frequency at the x - y -center of the ITO film (excitation from opposite inputs included); the dashed lines represent the complement of a normalized measure of the time-average intensity, defined as $1 - \left\{ \langle \|\tilde{\mathbf{E}}(t)\|^2 \rangle_T / \max \left[\langle \|\tilde{\mathbf{E}}(t)\|^2 \rangle_T \right] \right\} \{ 1 - \min [\omega_{p,h}(t)/\omega_p] \}$, at the same point, while the inset shows the second-harmonic ripples (see Appendix C).

the limit of negligible loss, perfect absorption could in principle be achieved, which would greatly boost the NTR.

Figure 4(b) depicts the flux of energy density across x at the output of the device, defined as $\Phi_x(y) = \int_{-\infty}^{\infty} \hat{\mathbf{x}} \cdot [\mathbf{E}(y, t) \times \mathbf{H}(y, t)] dt$ and normalized by the incident flux on the axis of the Gaussian beam, $\Phi_{0,x} = \sqrt{\pi} \sigma E_0^2 \cos \theta / 2\eta_0$. Integrating $\Phi_x(y)$ along y gives us the effective $|s_{21}|^2$ and $|s_{12}|^2$ shown in Fig. 3(b). The low-order harmonic distortion in the Kerr-like scenarios, which is only slightly perceptible in Fig. 4(a2) (solid and dashed blue lines), is much sharper in Fig. 4(c1), representing the output H_z at the y middle point. A Fourier transform of the Kerr outputs in Fig. 4(c1), included in Fig. 4(c2), shows a third and fifth harmonic, more pronounced when the device is excited from port 2 (dashed red line). Finally, Fig. 4(d) shows the time-varying $\omega_{p,h}(t)$ arising from the slow nonlinearity and its relaxation delay: the time delay between the minima of $\omega_{p,h}$ (solid lines) and the complement of the

normalized electric field intensity averaged over an optical cycle T (dashed lines) is around $25T$, or approximately 100 fs. Now, when $\omega_{p,h}$ is minimum, we have a maximum effective nonlinear change in the refractive index $\Delta n = 0.47 - 0.26i$. [In Appendix E, we present a study analogous to that shown in Fig. 4, but considering instead $E_0 = 692$ MV/m—indicated by the second black dashed line in Fig. 3. The stronger nonlinear response is evident when we inspect the higher-harmonic content caused by the fast nonlinearity and the larger dip in $\omega_{p,h}(t)$ arising from the slow nonlinearity, associated with a maximum $\Delta n = 0.88 - 0.34i$.]

V. CONCLUSIONS

We show theoretically how a simple thin two-layer stack comprising highly doped ITO and silicon provides the spatial asymmetry and, at the ENZ condition, the strong

nonlinear response necessary to break reciprocity. The large field confinement inside the ITO film is ultimately behind the enlarged nonreciprocal transmission, and, consequently, there is an upper limit on the NTR: as the effective nonlinear response increases (due to either an intrinsically larger nonlinear susceptibility or a higher incident power), this asymmetric mode confinement tends to disappear, thus killing the nonreciprocity. We show how this limiting mechanism is triggered above a similar input power level, regardless of the nature of the nonlinearity (instantaneous or thermal). The only open avenue left for increasing the nonreciprocal response would be to reduce the loss and thus decrease the denominator in the NTR, rather than increasing the numerator.

ACKNOWLEDGMENTS

This work is supported in part by the Defense Advanced Research Projects Agency (DARPA) Defense Sciences Office (DSO) Nascent Light-Matter Interaction Program under Grant No. W911NF-18-0369.

APPENDIX A: LINEAR DESIGN OF THE SI-ITO BILAYER: MAXIMIZATION OF ABSORPTION AND $|E_x|$

As pointed out in Sec. III, we seek to maximize the nonlinear response and, in turn, the NTR, by first achieving

optimal coupling to a Berreman mode sustained in our bilayer device in the vicinity of the ENZ frequency. We do so by first performing a linear TMM-based parametric sweep of both D_{Si} and D_{ITO} , with the pair (absorption, $|E_x|$) as the objective function for maximization when the ITO side (port 2) is fed. This is shown in Fig. 5, in which a Drude-Sommerfeld model parameterizes the linear dielectric function of ITO as $\epsilon(\omega) = \epsilon_\infty + \chi^{(1)}(\omega)$, where $\chi^{(1)}(\omega) = -\omega_p^2/(\omega^2 + i\omega\Gamma)$, with a free-electron linear plasma frequency $\omega_p = 2.9719 \times 10^{15}$ rad/s, a collision rate $\Gamma = 0.0468\omega_p$, and a high-frequency permittivity $\epsilon_\infty = 3.8055$, placing the ENZ condition at a wavelength of 1240 nm ($\epsilon_{\text{ENZ}} = 0.35i$) [49]. By inspecting Figs. 5(b1) and 5(b2), we can see that an absorptance peak of 0.83 is located at $D_{\text{Si}} \approx 80$ nm and $D_{\text{ITO}} \approx 100$ nm when the angle of incidence is between 40° and 55° .

APPENDIX B: EFFECT OF LOSS ON EFFICIENCY

In Fig. 6, we show the result of repeating the same calculations as in Fig. 2 when the collision frequency is reduced by 1 order of magnitude ($\Gamma = 0.00468\omega_p$), which allows us to achieve a similar maximum $|s_{12,nl}|^2/|s_{21,nl}|^2$ ratio of 2.15 at $(\lambda, \theta) \approx (1234 \text{ nm}, 22^\circ)$, but with $E_0 = 6.06 \times 10^6$ V/m, i.e., 200 times less intensity. This is consonant with the higher Q factor of the new quasiresonant device, which in the linear problem provides a backward-direction

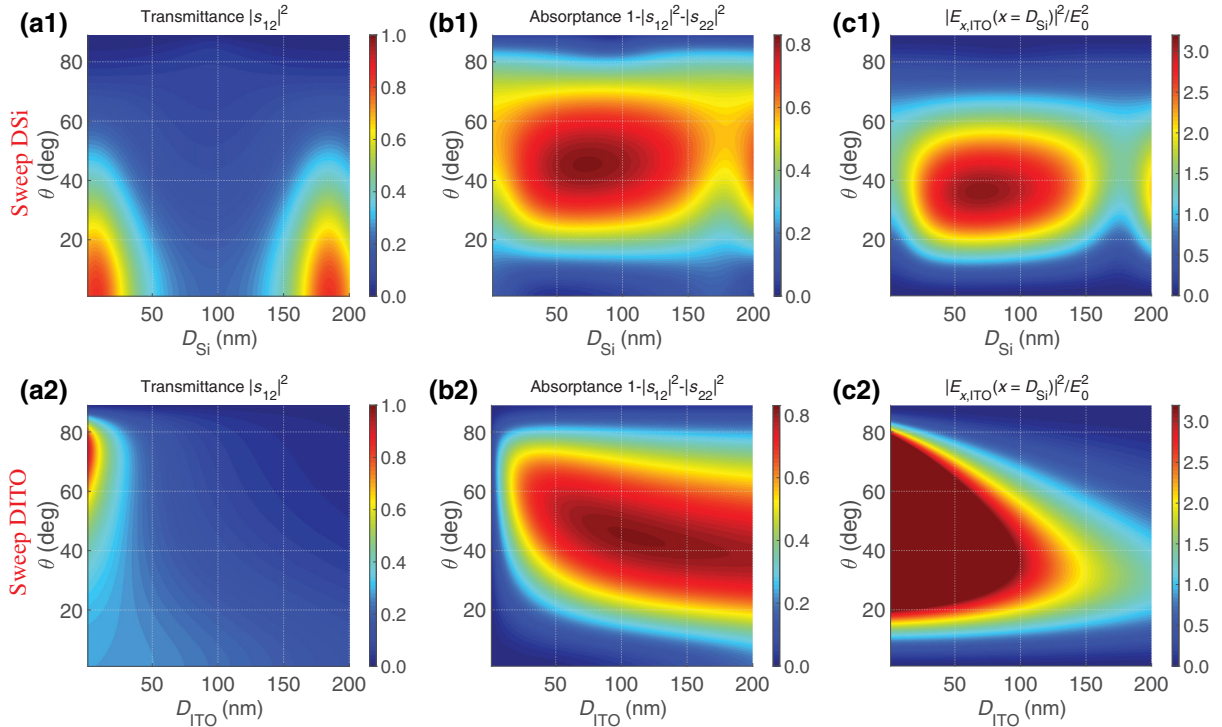


FIG. 5. Optimal values of Si and ITO film thicknesses from analysis of the linear problem for excitation from the ITO-layer side (port 2). (a1)–(c1) Transmittance, absorptance, and normalized (squared) longitudinal electric field magnitude $|E_x(x = D_{\text{Si}})|$, respectively, at the ITO side of the ITO-Si interface, versus Si film thickness D_{Si} and angle of incidence θ , for fixed $D_{\text{ITO}} = 100$ nm. (a2)–(c2) map the same quantities versus (D_{ITO}, θ) for $D_{\text{Si}} = 80$ nm.

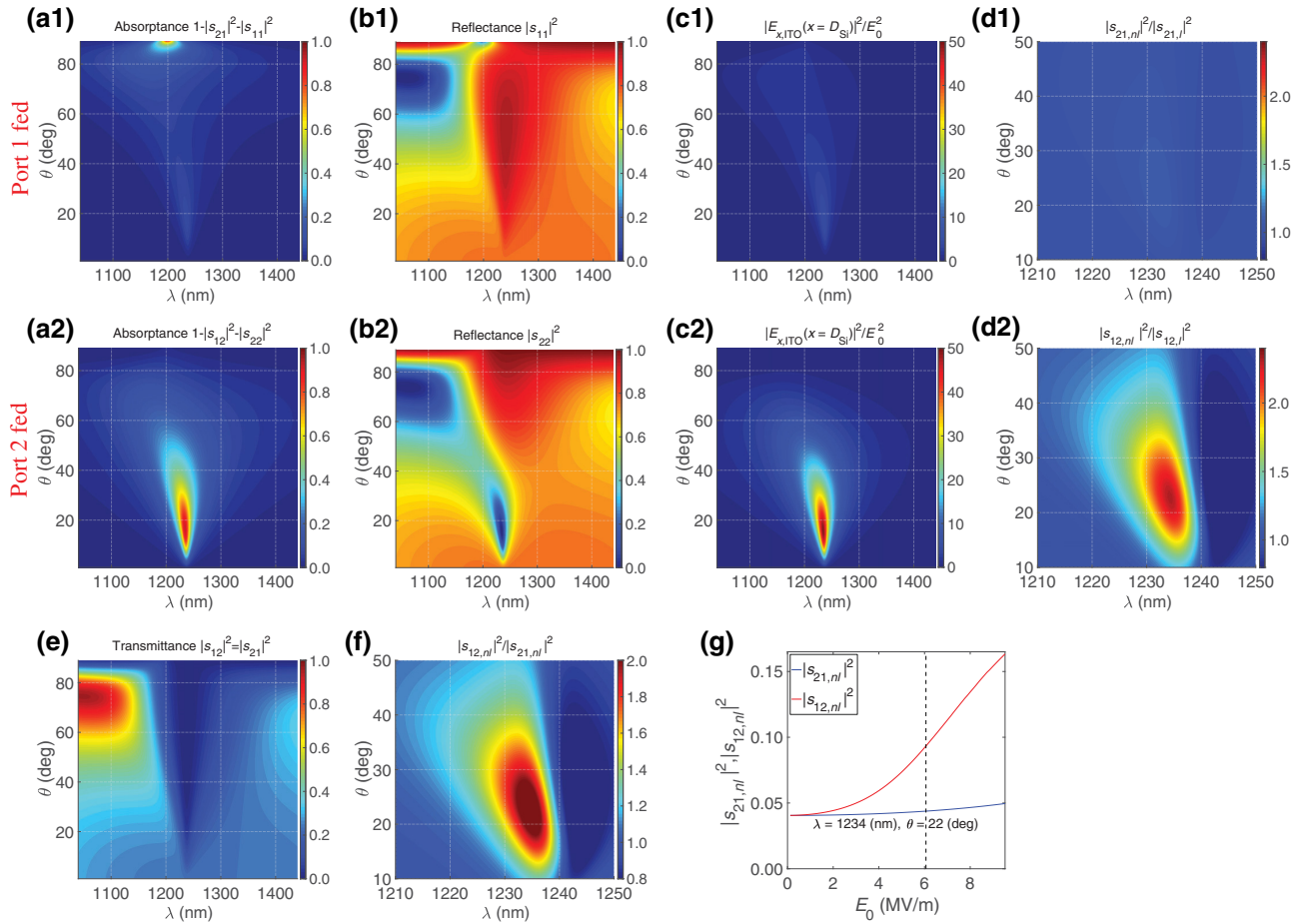


FIG. 6. Nonlinearity-induced nonreciprocal response versus (λ, θ) if we assume that the collision rate Γ in ITO is ten times smaller. The figure parts are the same as in Fig. 2.

narrow absorption peak of 0.93 and a $|E_x|^2$ enhancement above 50.

Furthermore, Fig. 7 shows the results obtained from replicating the numerical experiment shown in Fig. 3 but for continuous-wave plane-wave incidence, using both the original Γ and $\Gamma/10$. Irrespective of the nature of the nonlinearity (see Appendix C), the NTR decreases beyond a certain laser intensity, as seen in Fig. 3, and, notably, not only can this NTR peak be greatly boosted by reducing Γ , but also this peak is found at a lower light intensity.

APPENDIX C: NONPARABOLICITY OF ITO CONDUCTION BAND

On the one hand, there is experimental evidence of strong harmonic generation in quasiresonant ITO thin films under oblique excitation, which can be explained only by an instant nonlinear effect, very much like that of anharmonic oscillations of bound electrons in dielectric materials. Certainly, the free electrons in ITO are driven by the optical field within a nonparabolic energy band with an energy (\mathcal{E})–wave-vector (k) dispersion relation of the form

$\hbar^2 k^2/2m^* = \mathcal{E} + C\mathcal{E}^2$, C being the nonparabolicity parameter [62] and m^* the effective mass of the free electrons at the bottom of the conduction band ($k = 0$). The third-order susceptibility of this fast nonlinearity has been estimated to be roughly of the same order as nonresonant nonlinearities arising from bound electrons, around $10^{-19} (\text{V/m})^{-2}$ [33].

On the other hand, delayed nonlinearities involving real transitions, with a much stronger response, are behind the remarkably large nonlinear refractive index of ITO observed in Ref. [49]. This phenomenon can also be traced back to the nonparabolicity of the conduction band: the laser-induced absorption increases the temperature of the free carriers, some of which are promoted above the Fermi level, thus acquiring a higher effective mass. This is explained by the fact that electron density conservation in intraband transitions lowers the electrochemical potential, which, in turn, due to the nonparabolicity of the band, raises the effective mass of the sea of thermalized electrons at higher energy levels, which ultimately reduces the effective plasma frequency in our Drude model. Now, for degenerately doped TCOs, we can assume that the thermal energy of the electrons is well below a Fermi level

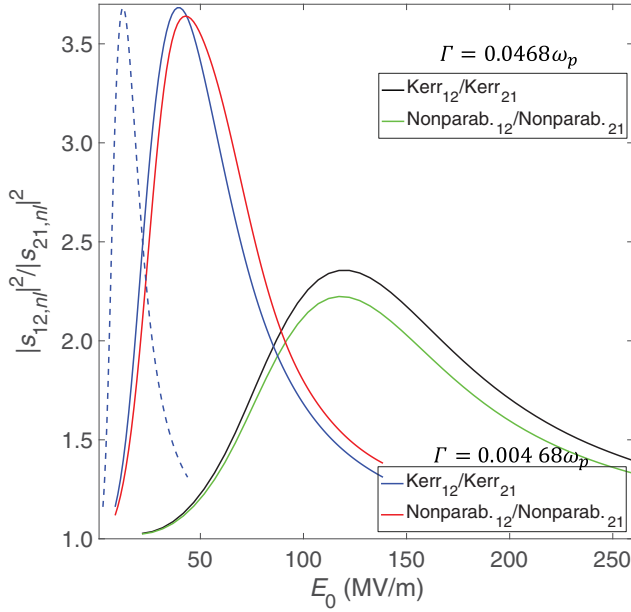


FIG. 7. Nonlinear transmittance ratio versus incident electric field magnitude for $\Gamma = 0.0468\omega_p$ (black and green lines) and $\Gamma = 0.00468\omega_p$ (red and blue lines), each at the corresponding optimal point in the (λ, θ) plane. Both fast and slow ITO nonlinearities are considered. When $\Gamma = 0.00468\omega_p$, the effective thermal susceptibility is reduced according to $\chi_{\text{eff}}^{(3)} \propto \Gamma$ [Eq. (C3)], and so we scale the fast susceptibility $\chi^{(3)}$ too (solid blue line). If, on the contrary, we keep the initial value of $\chi^{(3)} = 6.67 \times 10^{-18} (\text{V/m})^{-2}$, we have the same function compressed by a factor of $\sqrt{10}$ along the E_0 axis (dashed blue line). These calculations are performed for steady-state plane-wave excitation in the time domain.

of approximately 1 eV (i.e., the ratio $\kappa = U_h/N\mathcal{E}_F \ll 1$, where U_h is the thermal energy density, N is the electron volumetric density, and \mathcal{E}_F is the Fermi energy), which allows us to approximate the average effective mass of the electron gas as the effective mass at the Fermi level [33] and get by without the delayed two-temperature model [63] to describe the evolution of U_h as

$$\frac{dU_h(\mathbf{r}, t)}{dt} = \mathbf{J}(\mathbf{r}, t) \cdot \mathbf{E}(\mathbf{r}, t) - \frac{U_h(\mathbf{r}, t)}{\tau_{e\text{-ph}}}, \quad (\text{C1})$$

where the electron-phonon relaxation time $\tau_{e\text{-ph}}$ is only a few hundreds of femtoseconds (we assume $\tau_{e\text{-ph}} = 100$ fs), which explains the ultrafast response of this “slow” nonlinearity [64]. The nonparabolicity-induced “hot” nonlinear plasma frequency can thus be written as

$$\omega_{p,h}^2(\mathbf{r}, t) \approx \frac{\omega_p^2}{1 + \kappa(\mathbf{r}, t)} \approx \omega_p^2 [1 - \kappa(\mathbf{r}, t)], \quad (\text{C2})$$

which intrinsically embodies the saturation effect observed in, e.g., Ref. [49], and where the Taylor expansion—correct to first order—of the second equality allows

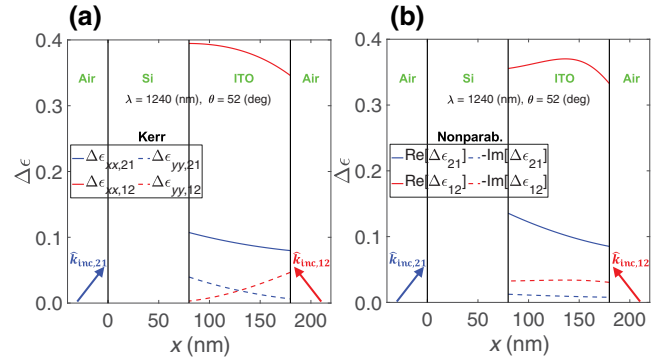


FIG. 8. Comparison of the effective nonlinear permittivity $\Delta\epsilon$ versus depth into the ITO film at the optimal (λ, θ) point of maximum NTR in Fig. 2(f), considering both Kerr (a) and thermal (b) nonlinearities: similar values of $\Delta\epsilon$ are obtained for both types of nonlinear interactions. Incidence from port 1 (blue) and port 2 (red) is included in both parts.

a straightforward parameterization of an effective nonlinear susceptibility in the continuous-wave scenario:

$$\chi_{\text{eff}}^{(3)}(\omega; \omega, -\omega, \omega) \approx -\epsilon_0 \chi^{(1)}(\omega) \frac{2\Gamma \tau_{e\text{-ph}} \omega_p^2}{(\omega^2 + \Gamma^2) N \mathcal{E}_F}. \quad (\text{C3})$$

If we assume that the average effective mass m_{eff} is 0.4 times the electron mass [65], we obtain $N = \epsilon_0 m_{\text{eff}} \omega_p^2 / q^2 = 1.11 \times 10^{21} \text{ cm}^{-3}$, which, from Eq. (C3), finally yields $\chi_{\text{eff}}^{(3)} = (2.00 - 0.18) \times 10^{-17} (\text{V/m})^{-2}$. In Sec. III, we use $\chi^{(3)} = \text{Re}[\chi_{\text{eff}}^{(3)}]/3$, taking into account the degeneracy factor 3. Rigorously speaking, however, we should note that whereas the nonlinear term in the dielectric function is now simply a scalar $\Delta\epsilon = \chi_{\text{eff}}^{(3)} \|\tilde{\mathbf{E}}(\mathbf{r}, \omega)\|^2$, in the previous section we have a second-order tensor described by $\Delta\epsilon_{xx} = 3\chi^{(3)} |\tilde{E}_x(\mathbf{r}, \omega)|^2$ and $\Delta\epsilon_{yy} = 3\chi^{(3)} |\tilde{E}_y(\mathbf{r}, \omega)|^2$, with $\Delta\epsilon_{yy} \ll \Delta\epsilon_{xx} \approx \Delta\epsilon$. This difference, illustrated in Fig. 8, has barely any effect on the nonlinear transmitted signal and the NTR maps.

Note also that only for a pulsed excitation does the delay effect of $1/(i\omega - \tau_{e\text{-ph}}^{-1})$ [33] obtained from Eq. (C1) emerge in this thermal nonlinearity [see Figs. 4(d) and 9(d)]; in a steady state, it instead manifests itself as a mere limiting factor as in Eq. (C3). Incidentally, from the dissipated power density $\mathbf{J} \cdot \mathbf{E}$ in Eq. (C1), U_h not only follows the pulse intensity but also acquires a comparatively small signal oscillating at twice the carrier frequency 2ω [see enlarged inset in Figs. 4(d) and 9(d)].

APPENDIX D: PARAMETERS OF THE SPACE-TIME-PULSED GAUSSIAN BEAM

For the results in Figs. 3 and 4, we adopt the paraxial approximation to the TEM_{00} Gaussian beam mode [66] in two dimensions (a beam-waist radius $w_0 = 4\lambda$ is used; the device length in the \mathbf{y} dimension is $16w_0$, enough to

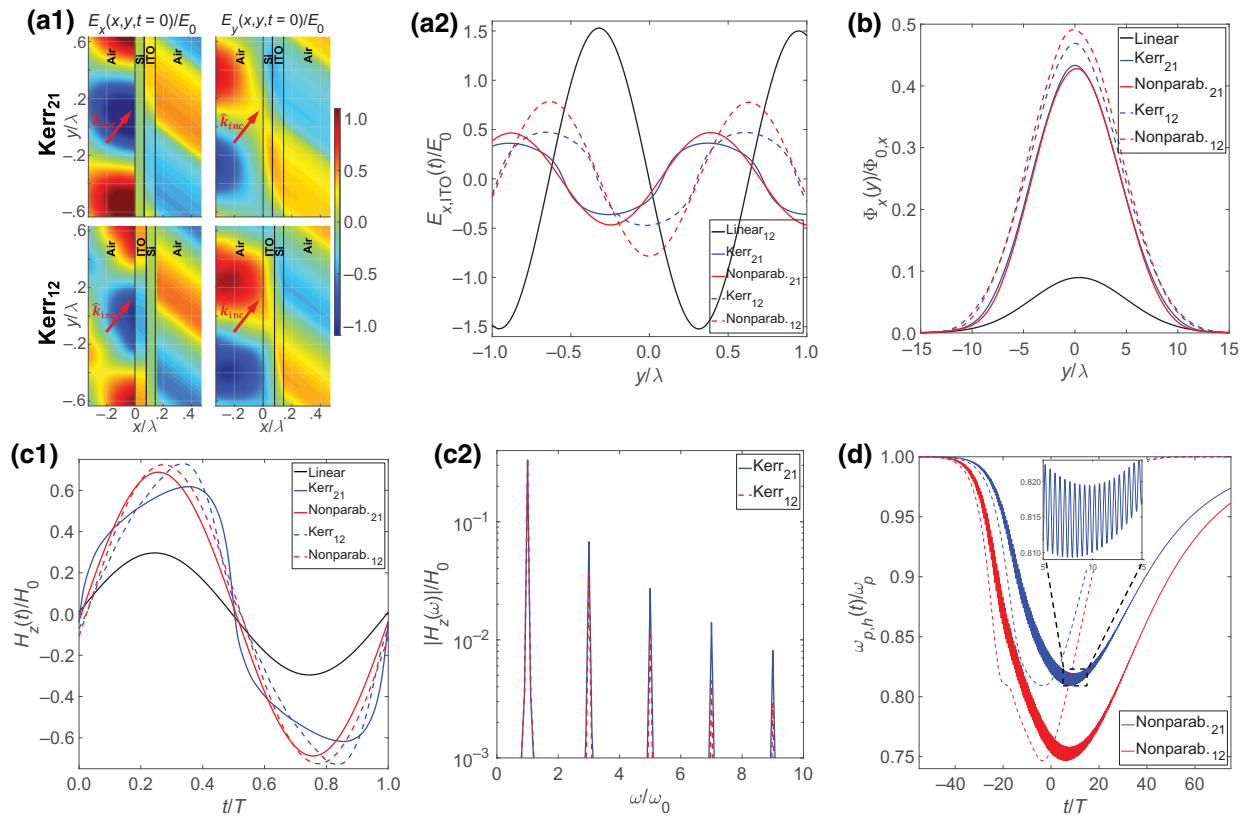


FIG. 9. Nonlinear response of the nonreciprocal device in the saturation regime (low NTR): $E_0 = 692$ MV/m. The figure parts are the same as in Fig. 4.

avoid edge effects), and modulate it with a Gaussian pulse signal $e^{-(t/\sigma)^2/2}$. As we choose $\sigma = 75$ fs, the bandwidth of the spectrum of the temporal Gaussian pulse is much smaller than the carrier frequency for near-infrared light, i.e., $1/\sigma \ll \omega$, and we can neglect the coupling among the beam parameters in space and time [67].

APPENDIX E: SATURATION OF THE NONLINEAR RESPONSE

The numerical analysis illustrated in Fig. 4 is repeated, replacing the incident electric field $E_0 = 195$ MV/m with $E_0 = 692$ MV/m, and the results are shown in Fig. 9. The stronger (saturated) nonlinear response comes at the expense of a large decay in the nonreciprocal response.

[1] H. B. G. Casimir, On Onsager's principle of microscopic reversibility, *Rev. Mod. Phys.* **17**, 343 (1945).
 [2] Z. Wang, Y. Chong, J. D. Joannopoulos, and M. Soljačić, Observation of unidirectional backscattering-immune topological electromagnetic states, *Nature* **461**, 772 (2009).
 [3] T. Amemiya, K. Abe, T. Tanemura, T. Mizumoto, and Y. Nakano, Nonreciprocal polarization conversion in

asymmetric magneto-optic waveguide, *IEEE J. Quantum Electron.* **46**, 1662 (2010).

[4] P. K. Jain, Y. Xiao, R. Walsworth, and A. E. Cohen, Surface plasmon resonance enhanced magneto-optics (SuPREMO): Faraday rotation enhancement in gold-coated iron oxide nanocrystals, *Nano Lett.* **9**, 1644 (2009).
 [5] T. Kodera, D. L. Sounas, and C. Caloz, Artificial Faraday rotation using a ring metamaterial structure without static magnetic field, *Appl. Phys. Lett.* **99**, 031114 (2011).
 [6] Z. Wang, Z. Wang, J. Wang, B. Zhang, J. Huangfu, J. D. Joannopoulos, M. Soljačić, and L. Ran, Gyrotropic response in the absence of a bias field, *Proc. Natl. Acad. Sci.* **109**, 13194 (2012).
 [7] Z. Yu and S. Fan, Complete optical isolation created by indirect interband photonic transitions, *Nat. Photonics* **3**, 91 (2009).
 [8] H. Lira, Z. Yu, S. Fan, and M. Lipson, Electrically Driven Nonreciprocity Induced by Interband Photonic Transition on a Silicon Chip, *Phys. Rev. Lett.* **109**, 033901 (2012).
 [9] D. L. Sounas, C. Caloz, and A. Alù, Giant non-reciprocity at the subwavelength scale using angular momentum-biased metamaterials, *Nat. Commun.* **4**, 2407 (2013).
 [10] D. L. Sounas and A. Alù, Angular-momentum-biased nanorings to realize magnetic-free integrated optical isolation, *ACS Photonics* **1**, 198 (2014).
 [11] L. D. Tzuang, K. Fang, P. Nussenzeig, S. Fan, and M. Lipson, Non-reciprocal phase shift induced by an effective magnetic flux for light, *Nat. Photonics* **8**, 701 (2014).

- [12] Z. Shen, Y.-L. Zhang, Y. Chen, C.-L. Zou, Y.-F. Xiao, X.-B. Zou, F.-W. Sun, G.-C. Guo, and C.-H. Dong, Experimental realization of optomechanically induced non-reciprocity, *Nat. Photonics* **10**, 657 (2016).
- [13] N. Chamanara, S. Taravati, Z.-L. Deck-Léger, and C. Caloz, Optical isolation based on space-time engineered asymmetric photonic band gaps, *Phys. Rev. B* **96**, 155409 (2017).
- [14] D. L. Sounas and A. Alù, Non-reciprocal photonics based on time modulation, *Nat. Photonics* **11**, 774 (2017).
- [15] M. Soljačić, C. Luo, J. D. Joannopoulos, and S. Fan, Nonlinear photonic crystal microdevices for optical integration, *Opt. Lett.* **28**, 637 (2003).
- [16] L. Fan, J. Wang, L. T. Varghese, H. Shen, B. Niu, Y. Xuan, A. M. Weiner, and M. Qi, An all-silicon passive optical diode, *Science* **335**, 447 (2012).
- [17] A. M. Mahmoud, A. R. Davoyan, and N. Engheta, All-passive nonreciprocal metastructure, *Nat. Commun.* **6**, 8359 (2015).
- [18] T. T. Koutserimpas and R. Fleury, Nonreciprocal Gain in Non-Hermitian time-Floquet Systems, *Phys. Rev. Lett.* **120**, 087401 (2018).
- [19] Y. Xu and A. E. Miroshnichenko, Reconfigurable nonreciprocity with a nonlinear Fano diode, *Phys. Rev. B* **89**, 134306 (2014).
- [20] Y. Yu, Y. Chen, H. Hu, W. Xue, K. Yvind, and J. Mork, Nonreciprocal transmission in a nonlinear photonic-crystal Fano structure with broken symmetry, *Laser Photon. Rev.* **9**, 241 (2015).
- [21] L. D. Bino, J. M. Silver, M. T. M. Woodley, S. L. Stebbings, X. Zhao, and P. Del’Haye, Microresonator isolators and circulators based on the intrinsic nonreciprocity of the Kerr effect, *Optica* **5**, 279 (2018).
- [22] K. Y. Yang, J. Skarda, M. Cotrufo, A. Dutt, G. H. Ahn, M. Sawaby, D. Vercruyssen, A. Arbabian, S. Fan, A. Alù, and J. Vučković, Inverse-designed non-reciprocal pulse router for chip-based lidar, *Nat. Photonics* **14**, 369 (2020).
- [23] M. Cotrufo, S. A. Mann, H. Moussa, and A. Alù, Nonlinearity-induced nonreciprocity—part I, *IEEE Trans. Microw. Theory Tech.* **69**, 3569 (2021).
- [24] M. Cotrufo, S. A. Mann, H. Moussa, and A. Alù, Nonlinearity-induced nonreciprocity—part II, *IEEE Trans. Microw. Theory Tech.* **69**, 3584 (2021).
- [25] H. Ramezani, T. Kottos, R. El-Ganainy, and D. N. Christodoulides, Unidirectional nonlinear \mathcal{PT} -symmetric optical structures, *Phys. Rev. A* **82**, 043803 (2010).
- [26] L. Chang, X. Jiang, S. Hua, C. Yang, J. Wen, L. Jiang, G. Li, G. Wang, and M. Xiao, Parity–time symmetry and variable optical isolation in active–passive-coupled microresonators, *Nat. Photonics* **8**, 524 (2014).
- [27] B. Jin and C. Argyropoulos, in *Photonic and Phononic Properties of Engineered Nanostructures X*, Vol. 11289, edited by A. Adibi, S.-Y. Lin, and A. Scherer: International Society for Optics and Photonics (SPIE, 2020), p. 1.
- [28] Y. Shi, Z. Yu, and S. Fan, Limitations of nonlinear optical isolators due to dynamic reciprocity, *Nat. Photonics* **9**, 388 (2015).
- [29] D. Jalas, A. Petrov, M. Eich, W. Freude, S. Fan, Z. Yu, R. Baets, M. Popović, A. Melloni, J. D. Joannopoulos, M. Vanwolleghem, C. R. Doerr, and H. Renner, What is — and what is not — an optical isolator, *Nat. Photonics* **7**, 579 (2013).
- [30] K. Xia, F. Nori, and M. Xiao, Cavity-Free Optical Isolators and Circulators Using a Chiral Cross-Kerr Nonlinearity, *Phys. Rev. Lett.* **121**, 203602 (2018).
- [31] E.-Z. Li, D.-S. Ding, Y.-C. Yu, M.-X. Dong, L. Zeng, W.-H. Zhang, Y.-H. Ye, H.-Z. Wu, Z.-H. Zhu, W. Gao, G.-C. Guo, and B.-S. Shi, Experimental demonstration of cavity-free optical isolators and optical circulators, *Phys. Rev. Res.* **2**, 033517 (2020).
- [32] M. G. Coco, S. A. McDaniel, and G. Cook, Laser inscribed waveguide optical isolators in iron-doped lithium niobate, *Appl. Opt.* **60**, G139 (2021).
- [33] J. B. Khurgin, M. Clerici, and N. Kinsey, Fast and slow nonlinearities in epsilon-near-zero materials, *Laser Photon. Rev.* **15**, 2000291 (2021).
- [34] P. Guo, R. D. Schaller, J. B. Ketterson, and R. P. H. Chang, Ultrafast switching of tunable infrared plasmons in indium tin oxide nanorod arrays with large absolute amplitude, *Nat. Photonics* **10**, 267 (2016).
- [35] M. Z. Alam, S. A. Schulz, J. Upham, I. De Leon, and R. W. Boyd, Large optical nonlinearity of nanoantennas coupled to an epsilon-near-zero material, *Nat. Photonics* **12**, 79 (2018).
- [36] D. L. Sounas and A. Alù, Nonreciprocity based on nonlinear resonances, *IEEE Antennas Wirel. Propag. Lett.* **17**, 1958 (2018).
- [37] D. L. Sounas, J. Soric, and A. Alù, Broadband passive isolators based on coupled nonlinear resonances, *Nat. Electron.* **1**, 113 (2018).
- [38] D. L. Sounas and A. Alù, Time-Reversal Symmetry Bounds on the Electromagnetic Response of Asymmetric Structures, *Phys. Rev. Lett.* **118**, 154302 (2017).
- [39] K. X. Wang, Z. Yu, S. Sandhu, and S. Fan, Fundamental bounds on decay rates in asymmetric single-mode optical resonators, *Opt. Lett.* **38**, 100 (2013).
- [40] D. L. Sounas and A. Alù, Fundamental bounds on the operation of Fano nonlinear isolators, *Phys. Rev. B* **97**, 115431 (2018).
- [41] D. M. Solís, R. W. Boyd, and N. Engheta, Dependence of the efficiency of the nonlinear-optical response of materials on their linear permittivity and permeability, *Laser Photon. Rev.* **15**, 2100032 (2021).
- [42] J. E. Sipe, New Green-function formalism for surface optics, *J. Opt. Soc. Am. B* **4**, 481 (1987).
- [43] D. M. Pozar, *Microwave Engineering* (John Wiley & Sons, Hoboken, NJ, 2011).
- [44] R. W. Boyd, *Nonlinear Optics, Third Editions* (Academic Press, Inc., Orlando, FL, USA, 2008), 3rd ed.
- [45] T. Szarvas and Z. Kis, Numerical simulation of nonlinear second harmonic wave generation by the finite difference frequency domain method, *J. Opt. Soc. Am. B* **35**, 731 (2018).
- [46] R. M. Joseph and A. Taflove, FDTD Maxwell’s equations models for nonlinear electrodynamics and optics, *IEEE Trans. Antennas Propag.* **45**, 364 (1997).
- [47] A. Capretti, Y. Wang, N. Engheta, and L. D. Negro, Enhanced third-harmonic generation in Si-compatible epsilon-near-zero indium tin oxide nanolayers, *Opt. Lett.* **40**, 1500 (2015).

- [48] L. Caspani, R. P. M. Kaipurath, M. Clerici, M. Ferrera, T. Roger, J. Kim, N. Kinsey, M. Pietrzyk, A. Di Falco, V. M. Shalaev, A. Boltasseva, and D. Faccio, Enhanced Nonlinear Refractive Index in ϵ -Near-Zero Materials, *Phys. Rev. Lett.* **116**, 233901 (2016).
- [49] M. Z. Alam, I. De Leon, and R. W. Boyd, Large optical nonlinearity of indium tin oxide in its epsilon-near-zero region, *Science* **352**, 795 (2016).
- [50] T. S. Luk, D. de Ceglia, S. Liu, G. A. Keeler, R. P. Prasankumar, M. A. Vincenti, M. Scalora, M. B. Sinclair, and S. Campione, Enhanced third harmonic generation from the epsilon-near-zero modes of ultrathin films, *Appl. Phys. Lett.* **106**, 151103 (2015).
- [51] A. Capretti, Y. Wang, N. Engheta, and L. Dal Negro, Comparative study of second-harmonic generation from epsilon-near-zero indium tin oxide and titanium nitride nanolayers excited in the near-infrared spectral range, *ACS Photonics* **2**, 1584 (2015).
- [52] Y. Yang, J. Lu, A. Manjavacas, T. S. Luk, H. Liu, K. Kelley, J.-P. Maria, E. L. Runnerstrom, M. B. Sinclair, S. Ghimire, and I. Brener, High-harmonic generation from an epsilon-near-zero material, *Nat. Phys.* **15**, 1022 (2019).
- [53] S. Campione, D. de Ceglia, M. A. Vincenti, M. Scalora, and F. Capolino, Electric field enhancement in ϵ -near-zero slabs under TM-polarized oblique incidence, *Phys. Rev. B* **87**, 035120 (2013).
- [54] H. Lu, T. Zhu, J. Zhang, H.-C. Liu, K.-S. Shen, Y. Zheng, S.-Q. Dong, S.-Q. Xia, C. Dong, X.-K. Li, W.-Y. Luo, X.-L. Sun, X.-Z. Zhang, and C.-H. Xue, Nonreciprocal tamm plasmon absorber based on lossy epsilon-near-zero materials, *Opt. Express* **29**, 17736 (2021).
- [55] S. Vassant, J.-P. Hugonin, F. Marquier, and J.-J. Greffet, Berreman mode and epsilon near zero mode, *Opt. Express* **20**, 23971 (2012).
- [56] T. S. Luk, S. Campione, I. Kim, S. Feng, Y. C. Jun, S. Liu, J. B. Wright, I. Brener, P. B. Catrysse, S. Fan, and M. B. Sinclair, Directional perfect absorption using deep subwavelength low-permittivity films, *Phys. Rev. B* **90**, 085411 (2014).
- [57] D. L. Sounas, Virtual perfect absorption through modulation of the radiative decay rate, *Phys. Rev. B* **101**, 104303 (2020).
- [58] R. W. Ziolkowski, J. M. Arnold, and D. M. Gogny, Ultrafast pulse interactions with two-level atoms, *Phys. Rev. A* **52**, 3082 (1995).
- [59] N. Kinsey, C. DeVault, A. Boltasseva, and V. M. Shalaev, Near-zero-index materials for photonics, *Nat. Rev. Mater.* **4**, 742 (2019).
- [60] R. Secondo, J. Khurgin, and N. Kinsey, Absorptive loss and band non-parabolicity as a physical origin of large nonlinearity in epsilon-near-zero materials, *Opt. Mater. Express* **10**, 1545 (2020).
- [61] M. A. Vincenti, D. de Ceglia, J. W. Haus, and M. Scalora, Harmonic generation in multiresonant plasma films, *Phys. Rev. A* **88**, 043812 (2013).
- [62] E. O. Kane, Band structure of indium antimonide, *J. Phys. Chem. Solids* **1**, 249 (1957).
- [63] E. Carpene, Ultrafast laser irradiation of metals: Beyond the two-temperature model, *Phys. Rev. B* **74**, 024301 (2006).
- [64] N. Kinsey, C. DeVault, J. Kim, M. Ferrera, V. M. Shalaev, and A. Boltasseva, Epsilon-near-zero Al-doped ZnO for ultrafast switching at telecom wavelengths, *Optica* **2**, 616 (2015).
- [65] X. Liu, J. Park, J.-H. Kang, H. Yuan, Y. Cui, H. Y. Hwang, and M. L. Brongersma, Quantification and impact of non-parabolicity of the conduction band of indium tin oxide on its plasmonic properties, *Appl. Phys. Lett.* **105**, 181117 (2014).
- [66] M. Katsav and E. Heyman, Gaussian beam summation representation of a two-dimensional gaussian beam diffraction by a half plane, *IEEE Trans. Antennas Propag.* **55**, 2247 (2007).
- [67] Zhongyang Wang, Zhengquan Zhang, Zhizhan Xu, and Qiang Lin, Space-time profiles of an ultrashort pulsed gaussian beam, *IEEE J. Quantum Electron.* **33**, 566 (1997).